Thin Solid Films 517 (2009) 2158–2162

Contents lists available at ScienceDirect

Thin Solid Films

journal homepage: www.elsevier.com/locate/tsf

Hydrazine-based deposition route for device-quality CIGS films

David B. Mitzi [a,*], Min Yuan [a], Wei Liu [a], Andrew J. Kellock [b], S. Jay Chey [a], Lynne Gignac [a], Alex G. Schrott [a]

[a] IBM T. J. Watson Research Center, P. O. Box 218, Yorktown Heights, NY 10598 USA
[b] IBM Almaden Research Center, 650 Harry Rd, San Jose, CA 95120 USA

ARTICLE INFO

Available online 6 November 2008

Keywords:
CIGS
Solar cells
Non-vacuum
Spin coating
Thin-film
Photovoltaics

ABSTRACT

A simple solution-based approach for depositing CIGS (Cu–In–Ga–Se/S) absorber layers is discussed, with an emphasis on film characterization, interfacial properties and integration into photovoltaic devices. The process involves incorporating all metal and chalcogenide components into a single hydrazine-based solution, spin coating a precursor film, and heat treating in an inert atmosphere, to form the desired CIGS film with up to micron-scaled film thickness and grain size. PV devices (glass/Mo/CIGS/CdS/i-ZnO/ITO) employing the spin-coated CIGS and using processing temperatures below 500 °C have yielded power conversion efficiencies of up to 10% (AM 1.5 illumination), without the need for a post-CIGS-deposition treatment in a gaseous Se source or a cyanide-based bath etch. Short-duration low-temperature (T<200 °C) oxygen treatment of completed devices is shown to have a positive impact on the performance of initially underperforming cells, thereby enabling better performance in devices prepared at temperatures below 500 °C.

1. Introduction

Low-cost processing techniques for photovoltaic (PV) device fabrication—especially for the active absorber layer—are critically needed to enable PV technology to become cost competitive with conventional electricity generation [1]. $Cu_{1-z}In_{1-x}Ga_xSe_{2-y}S_y$ (CIGS) represents one of the leading absorber layer candidates for achieving a cost competitive (on a $/W basis) thin-film technology, primarily because of the demonstrated potential for high power conversion efficiencies (up to ~20%) and for incorporating relatively high levels of device performance into a variety of useful form factors (e.g., building materials and mechanically flexible devices) [2,3]. Despite offering great promise, the complicated nature of this material generally renders the deposition process quite complex and therefore time consuming/costly. Most high-efficiency CIGS PV devices are deposited using multistep vacuum-based deposition processes (e.g., sputtering or evaporation) [4–6]. While reasonably low-cost CIGS solar modules can be produced using the vacuum-based techniques, the high initial capital investment for implementing these processes, coupled with uniformity issues over larger-scale substrates, has triggered a growing interest in developing potentially lower-cost solution-based CIGS deposition approaches [6–15].

Several solution-based approaches have been demonstrated for CIGS deposition, including electrochemical [7–9], spray or spin coating of organometallic precursors [10,11], screen printing of CIGS or component metal pastes [12,13], and printing of nanoparticle-based precursors [14,15]. A number of processing issues arise in these approaches, however, including: 1) removing undesirable film impurities that derive from the selected precursor and solvent (e.g., O, C, Cl), 2) getting rid of the need for a high-temperature post-deposition treatment in a gaseous selenium source (e.g., H_2Se) or in a cyanide-based bath, 3) simplifying or reducing the number of steps required to deposit high quality films, and 4) improving the compositional control and quality of the solution-processed CIGS films so that higher efficiency devices can be achieved. Here we focus on a new hydrazine-based precursor approach for depositing CIGS and related chalcogenide-based absorber layers [16]. Deposition involves dissolving the elements in a hydrazine-based solvent, spin coating the precursor solution into thin-film form, and heat treating the precursor film in an inert atmosphere to yield the targeted CIGS layer [16–19], with no need for high-temperature post-deposition selenization treatment [4] or a cyanide bath etch step [20] to correct phase purity, stoichiometry and grain size. In contrast to our earlier report [16], which focused on initial PV device results for films processed above 500 °C, this report will provide more detailed characterization of the CIGS films and interfaces, as well as demonstrate how low-temperature treatment in an oxygen atmosphere can improve the performance of the solution-deposited CIGS devices with processing temperatures constrained to T<500 °C.

2. Experimental details

All CIGS film processing was performed in a nitrogen-filled glove box with water and O_2 levels maintained below 1 ppm. Note that hydrazine is highly toxic and should be handled using appropriate protective equipment to prevent contact with either the vapors or liquid.

* Corresponding author. Tel.: +1 914 945 4176; fax: +1 914 945 2141.
E-mail address: dmitzi@us.ibm.com (D.B. Mitzi).

0040-6090/$ – see front matter
doi:10.1016/j.tsf.2008.10.079

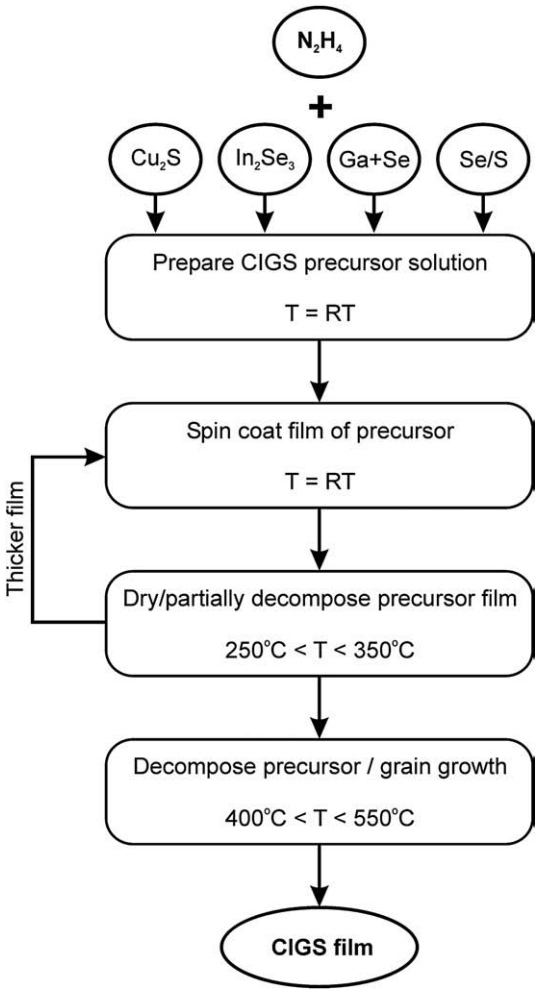

Fig. 1. Schematic flow diagram for the hydrazine-based CIGS deposition process.

2.1. Thin-film formation

CIGS ($Cu_{1-z}In_{1-x}Ga_xSe_{2-y}S_y$) precursor solutions were prepared by dissolving the components (i.e., Cu_2S, In_2Se_3, Ga, S, Se) in hydrazine at room temperature, as described in more detail in [16]. Extra Se was generally included in the solution to improve film morphology and to control the S:Se ratio in the resulting film. CIGS films were spin coated onto molybdenum-coated 2.5 cm×2.5 cm soda lime glass substrates (0.1 cm thickness) using the precursor solutions. The films were immediately dried and partially decomposed for 5 min at 290 °C on a preheated hot plate, followed by a final heat treatment at a selected temperature of between 400 and 500 °C. When thick (μm-scaled) films were desired for device structures, sequential layers were deposited using the same solution for each layer (typical film thickness per deposition layer is ~100 nm) [16].

2.2. Device fabrication

The device structure was formed on Mo-coated (~700-nm-thick layer) soda lime glass employing a ~1.3-μm-thick CIGS absorber layer, deposited as described above using 12 deposition cycles and a final heat treatment at 490 °C for 30 min. The device was completed with ~50 nm of chemical bath deposited CdS, 70 nm of sputtered intrinsic ZnO, followed by 200 nm of sputtered ITO (indium tin oxide). The sheet resistance of the ITO layer (on a glass slide without the other layers) was 50–60 Ω/sq, as measured using a 4-point probe method, and the transparency in the visible spectral range was >80%. Finally, a patterned Ni (50 nm)/Al (2 μm) grid was deposited on the top of the device to facilitate collecting the photo-

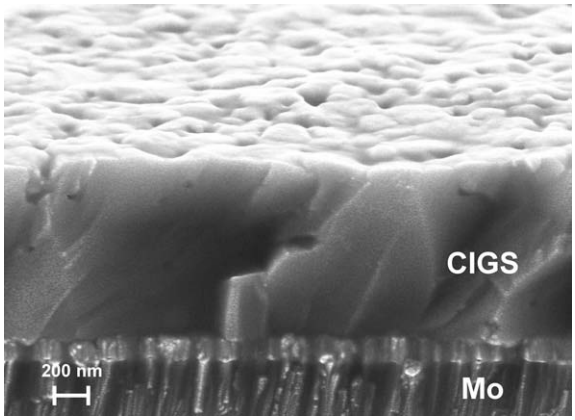

Fig. 2. Cross-sectional SEM image of a CIGS film, processed using 8 deposition cycles and a final 45 min heat treatment at 450 °C. Nominal film composition, as measured using RBS and PIXE, is $CuIn_{0.7}Ga_{0.3}Se_{1.9}S_{0.2}$. The experimental uncertainty in stoichiometry for each element is ~0.05.

generated carriers. Each device (0.45 cm^2 total area) was separated from neighboring devices (four per substrate) by mechanical scribing. Selected completed devices were further processed by annealing in a tube furnace at 180 °C under flowing O_2 for between 2 and 20 min to examine the effect of this treatment on device performance.

2.3. Characterization

For all device depositions, corresponding CIGS films deposited on oxidized silicon using the same spin-coating solution and deposition conditions were analyzed by a combination of RBS (Rutherford Backscattering Spectrometry) and PIXE (Particle Induced X-ray Emission) to verify that the targeted composition was obtained. RBS was performed using an NEC 3UH Pelletron, with a beam current of 20 nA at 2.3 MeV, while PIXE was performed using the same machine with 1.1 MeV protons. The PV devices were electrically tested using a Hewlett-Packard 4145B semiconductor analyzer under ambient temperature/atmosphere conditions. Simulated sunlight was applied using a 300 W (Xe lamp) Oriel Solar Simulator with AM1.5 filter. The light source was calibrated to 100 mW cm^{-2} using a NIST-calibrated Eppley thermopile, as well as an Oriel reference solar cell (NREL calibrated).

3. Results and discussion

3.1. Hydrazine-based deposition process

The first step of the hydrazine-based deposition process (shown schematically in Fig. 1) consists of dissolving each component metal

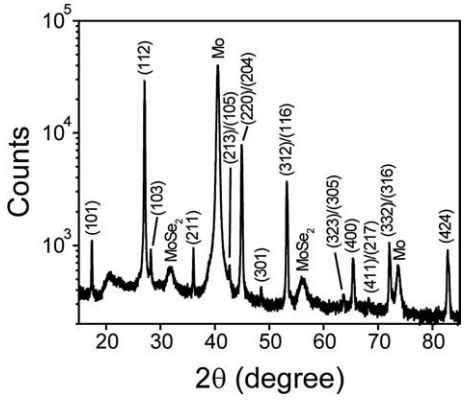

Fig. 3. Powder X-ray (Cu Kα radiation) diffraction from the solution-deposited CIGS film shown in Fig. 2, with reflection indices indicated for the CIGS phase.

chalcogenide (e.g., Cu_2S, In_2Se_3) or individual metal with chalcogen (e.g., Ga and Se) in anhydrous hydrazine at room temperature. By preparing separate solutions for each component, a range of film compositions can be readily achieved by mixing appropriate quantities of each component solution into the final all-inclusive spin-coating solution. The flexibility to quickly and conveniently prepare a full range of stoichiometries in the CIGS phase diagram facilitates the optimization process for the absorber layer. Importantly, the precursor solutions consist of only the elements found in CIGS (i.e., Cu, In, Ga, Se, S), as well as the weakly coordinating solvent hydrazine (N_2H_4), and therefore contaminants (e.g., C, O, Cl) are kept to a minimum in the deposited films. Due to the reactive nature of hydrazine [21], all processing must be conducted under inert atmosphere conditions, further reducing the probability of contaminant incorporation.

In step 2 (see Fig. 1), the precursor solutions are spin-coated onto a suitably prepared/cleaned substrate, with layer thickness being controlled by solution concentration, spin speed and ramp rate. Other solution-based thin-film deposition techniques (e.g., printing, spraying, dipping) might also be employed to deliver and dry the hydrazine-based solution onto a substrate to form the precursor film. Step 3 consists of heat treating the deposited precursor film so that excess hydrazine is removed from the sample and the resulting hydrazinium-based precursor is decomposed into the desired CIGS film. Drying begins during the spinning process and is completed during a short (5 min) low-temperature (typically 290 °C) heating, which is accomplished on a hot plate. During this low-temperature treatment, some decomposition of the precursor film will have commenced, but there is still a significant quantity of excess chalcogen (S, Se) left in the film, which does not fully dissociate from the film until temperatures of >300 °C [16]. The high temperature treatment (typically performed at 400 °C≤T≤550 °C for a period of between 10 min and 45 min) completes the transition from the hydrazinium precursor to single-phase CIGS and enables significant crystalline grain growth. Note that if thick or compositionally graded films are desired, multiple depositions are performed using either the same or a different composition solution to reach the desired thickness. Between the deposition of each layer, only the low-temperature treatment is performed, with the high-temperature treatment being used at the end after the deposition of all layers [16].

The simple hydrazine-based process offers several advantages over previously described solution-based CIGS deposition techniques. In contrast to nanoparticle-based techniques, in which nanoparticles of the component metals or metal oxides are first synthesized and then dispersed in solution [14,15] or the paste screen printing technique [12,13], in which μm-scaled chalcopyrite particles are typically dispersed in a solvent, the hydrazine-based approach relies on the formation of a true solution. The components are mixed on a molecular scale, thereby facilitating formation of a compositionally uniform CIGS phase at moderately low temperatures. All of the required elements are contained within one precursor solution and the desired phase can be achieved without the need to employ a post-deposition heat treatment in a chalcogen- and/or hydrogen-containing atmosphere [4,15], or the requirement to correct the film composition using physical vapor deposition [22] or a cyanide-based bath dip [20].

3.2. Deposited CIGS films and interfacial properties

A typical spin-coated film, prepared using a maximum temperature of 450 °C and a targeted composition of $CuIn_{0.7}Ga_{0.3}(Se,S)_2$, is shown in Fig. 2. Micron-scaled film thicknesses and grain dimensions are readily achieved, even at the relatively low processing temperature used (significantly less than 500 °C). X-ray diffraction from this film is shown in Fig. 3 and demonstrates the single-phase crystalline nature of the film, with the exception of peaks from the Mo undercoat and an interfacial Mo–Se rich layer [23]. The interfacial phase shows up in the diffraction pattern as two broad peaks at $2\theta \approx 32°$ and 56° (consistent with the (100) and (110) peaks from hexagonal $MoSe_2$), and is evident as a distinct layer between the CIGS and Mo layers in the SEM cross section of Fig. 2. The refined tetragonal lattices parameters for the CIGS phase, derived from the full diffraction pattern shown in Fig. 3, are $a=b=5.699(1)$ Å, $c=11.421(1)$ Å and $V=370.94$ Å^3, consistent with the expected values [16].

The formation of a Mo–Se-rich layer at the Mo/CIGS interface can provide an ohmic back contact as well as introduce a beneficial back surface electric field, as a result of the larger band gap relative to CIGS, and therefore represents an important factor for device operation [23,24]. Fig. 4 shows a TEM image of the CIGS/Mo interface from the same film depicted in Fig. 2, providing a clearer view of the interfacial phase forming between the Mo and CIGS layers. An energy dispersive spectroscopy (EDS) line scan, performed across the entire film thickness of a similarly prepared CIGS film (Fig. 5), highlights the compositional variation that occurs across this interface. The interfacial layer is rich in Mo and Se (and some Cu), but is deficient in In and Ga, consistent with this layer being $MoSe_2$-related, as described in [23]. Note that there is some tendency to form voids at the interface between the CIGS and the $MoSe_2$ phase, which might impact the adhesion between the CIGS and the substrate. The thickness of the interfacial layer can be influenced by the amount of extra S/Se added to the precursor solution, the heat treatment temperature used and the heat treatment duration. In Fig. 6a, for example, X-ray diffraction patterns are shown for two films processed using the same deposition conditions, but with different amounts of extra selenium added to the spin-coating solution (0.0 vs. 0.8 mol of extra Se added per mol of CIGS). Fig. 6b highlights the change in interfacial layer formation (as indicated by the change in X-ray intensity for this phase) using the same CIGS solution (0.8 mol of extra Se added) and 450 °C processing temperature, but different heat treatment durations. The amount of Na present in the CIGS layer has also previously been demonstrated to

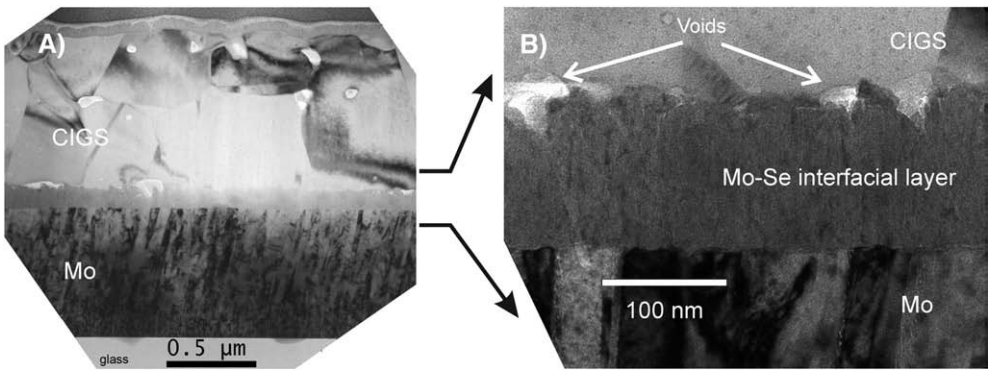

Fig. 4. A) Cross-sectional TEM image of the CIGS film shown in Fig. 2. B) Higher magnification image focusing on the interface region of the CIGS film. Note that this film was prepared with 0.8 mol of extra Se added to the precursor solution per mol of CIGS.

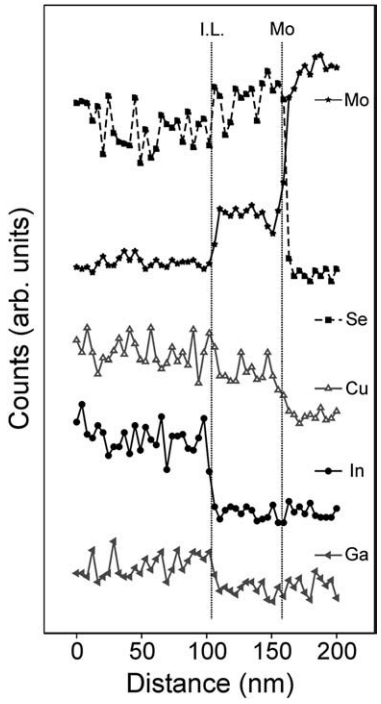

Fig. 5. Energy dispersive spectroscopy (EDS) line scans for Ga, In, Cu, Se and Mo, performed through the full thickness of a CIGS film. The film was prepared similarly to that used in Fig. 2, but with a final heat treatment at 450 °C for 20 min rather than for 45 min (leading to a thinner interfacial layer). The approximate positions of both the Mo and interfacial layer ("I.L.") interfaces are noted with dotted lines.

influence the thickness of the interfacial layer for vacuum deposited films and likely plays a role in the solution-processed films as well [23].

Besides the interfacial layer, the grain structure achieved within a given CIGS film depends sensitively on the thermal treatment (e.g., temperature, ramp rate, duration), the overall chemical composition of the film (e.g., particularly Cu poor verses Cu rich) and impurities introduced (either intentionally or not). Fig. 7a shows, for example, the grain structure for a Cu-poor film ($Cu_{0.92}In_{0.7}Ga_{0.3}Se_2$ targeted stoichiometry) processed at 450 °C. Note the significantly smaller grain structure compared with the stoichiometric film in Fig. 2. However, films processed using the same Cu-poor solution, but using higher temperature (485 °C and 525 °C) for the final heat treatment, demonstrate a significantly larger grain structure (Fig. 7b and c, respectively), thereby yielding suitable films for device fabrication. In addition to varying Cu content, we have previously shown that both gallium content and sulfur/selenium ratio can be continuously varied in $Cu_{1-z}In_{1-x}Ga_xSe_{2-y}S_y$ ($x<0.5$, $y<0.6$ and $z<0.15$), with a progressive change in structural and electronic properties in the solution-deposited CIGS films [16]. Note, however, that while Cu, In and Ga film stoichiometry can be controlled in a well-defined manner using the stoichiometry of the starting solution, the relationship between excess of S or Se used during the thin-film processing and the S:Se ratio in the final film is not as well defined, given the volatility of these elements during the heating process, and must be established empirically. By carefully tuning the film composition, films with suitable grain structure and composition can be tailored for PV device fabrication.

3.3. Thin-film device results

Recently, we reported initial solution-processed CIGS devices with an external power conversion efficiency of 10.3% (0.45 cm^2 total device area) [16]. While these devices were fabricated with peak processing temperature of 525 °C, here we consider glass/Mo/CIGS(solution-processed)/CdS/ZnO/ITO devices prepared using a lower-temperature final heat treatment of 490 °C, as well as the effect of post-fabrication oxygen annealing. The CIGS layer in these devices has the composition, $Cu_{0.90(5)}In_{0.69(5)}Ga_{0.29(5)}Se_{1.96(5)}S_{0.13(5)}$, as determined by RBS and PIXE analysis. Light (i.e., under 1 sun illumination) current–voltage (I–V) characteristics appear in Fig. 8 for all four as-deposited devices on the 1″×1″ substrate (dashed lines). The best device yields a short-circuit current density (J_{sc}), open-circuit voltage (V_{oc}), fill factor and total area power conversion efficiency of 22.3 (21.2–23.1) mA cm^{-2}, 560 (550–560) mV, 0.64 (0.63–0.64) and 8.1 (7.5–8.1) %, respectively, with the range of values observed over the four devices shown in parentheses. Presumably, at least in part, the inferior operational parameters, relative to the previously reported 525 °C-processed devices, result from a finer grain structure in the 490 °C-processed structures.

Low temperature air annealing has been previously used to improve the performance of CIGS-based PV devices, apparently as a result of passivation of Se vacancies at the grain boundaries and at the film surface [25,26]. In Fig. 8 (solid lines), the I–V curve for the same 490 °C "as made" films previously described are remeasured after 15 min of annealing at 180 °C in a flowing oxygen atmosphere followed by an open circuit light soak for 24 h (also know to improve device performance [27]). The best device offers a J_{sc}, V_{oc}, fill factor and total area power conversion efficiency of 24.6 (23.8–24.6) mA cm^{-2}, 590 (580–590) mV, 0.71 (0.69–0.71) and 10.1 (9.8–10.1) %, respectively, with the range of values observed over the four devices shown in parentheses. In this experiment, the improvement in J_{sc} is essentially entirely attributed to the oxygen anneal, whereas a small

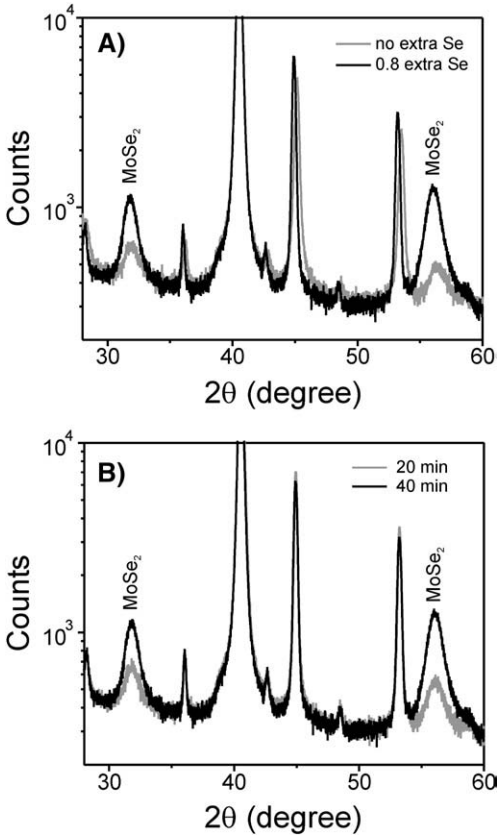

Fig. 6. Powder X-ray (Cu Kα radiation) diffraction from solution-deposited CIGS films with a targeted $CuIn_{0.7}Ga_{0.3}(Se,S)_2$ stoichiometry (RBS/PIXE confirmed), highlighting the formation of the $MoSe_2$ interfacial layer. In A) two films are deposited and compared from solutions that either had no extra Se added (gray curve) or 0.8 mol extra Se added (black curve) per mol of CIGS. In each case the films were heat treated at 450 °C for 40 min. In B) two films are compared, which were deposited using the same solution (0.8 mol extra Se added) and deposition conditions, but with either a 20 min (gray curve) or 40 min (black curve) final 450 °C heat treatment.

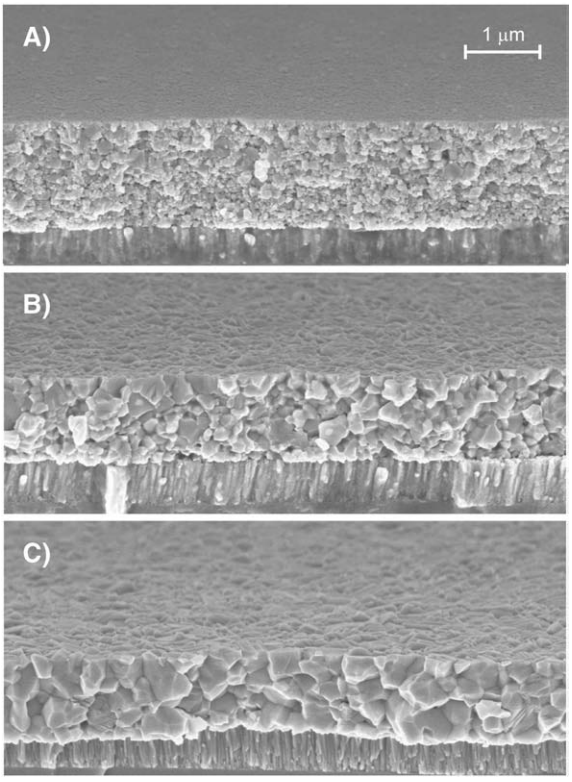

Fig. 7. Cross sectional SEM images of CIGS films with $Cu_{0.92}In_{0.7}Ga_{0.3}Se_2$ targeted stoichiometry and final processing temperatures: A) 450 °C for 30 min, B) 485 °C for 30 min, or C) 525 °C for 20 min. The same scale bar applies for each panel.

increase in V_{oc} was noted after the light soak treatment. The oxygen-annealed films in Fig. 8 have been remeasured after two months, with essentially no degradation of the device characteristics (i.e., all devices still operating in the 9–10% efficiency range). It should also be noted that the effect of oxygen annealing on devices that already operate at a reasonably high level of performance (i.e., power conversion efficiency of 9–10% or better) is generally not as striking as that shown in Fig. 8 and can even be detrimental. Oxygen annealing is therefore shown to provide a pathway to improve inferior device performance and enable lower-temperature hydrazine-processed devices to operate at a level comparable to those prepared at higher temperature.

4. Conclusions

One of the key benefits of the hydrazine-based deposition approach is the flexibility to tailor the composition/properties of the CIGS absorber layer simply by weighing out the different components on a balance before preparing the solution (or measuring selected volumes of pre-prepared solutions for each of the elements), enabling rapid testing over a wide range within the multi-component phase diagram. Composition not only affects the electronic properties (i.e., conductivity, band gap), but also the grain structure and interfacial properties of the spin-coated CIGS films on Mo-coated glass substrates. Using film composition, heat treatment duration/temperature, and post-deposition oxygen annealing/light soaking, PV devices have been fabricated with 10.1% external power conversion efficiency, using processing temperatures constrained below 500 °C. Given the early nature of this project, we believe that further efficiency enhancement should be possible as the device and absorber layer structure are further refined. Furthermore, as previously demonstrated [16–19], hydrazine-based deposition of chalcogenides is quite versatile and the process is expected to be extendable to the deposition of selected other prospective metal-chalcogenide-based absorber layers.

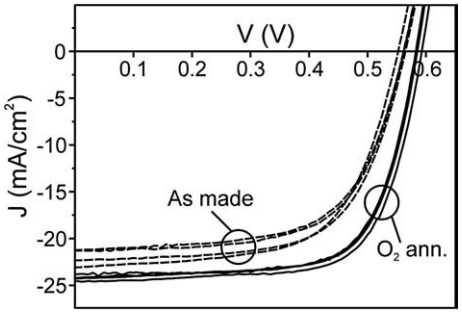

Fig. 8. Electrical characteristics of PV devices (Air Mass 1.5 illumination; 100 mW cm^{-2}; 0.45 cm^2 device area), prepared using the hydrazine-based approach and a final heat treatment at 490 °C. The dashed curves correspond to the results for four "as-prepared" devices (same substrate), while the solid curves correspond to the same devices after annealing in flowing O_2 at 180 °C for 15 min and light soaking at 1 sun intensity for 24 h.

Acknowledgments

The authors thank R. Ferlita and S. Rossnagel for technical support with the preparation of the Ni/Al grid and ZnO films, H. Hovel for technical assistance in performing the PV device measurements, S. Mittal for TEM sample preparation, and R. Noufi for providing the grid mask design used for this study.

References

[1] Basic Research Needs for Solar Energy Utilization, Report on the Basic Energy Sciences Workshop on Solar Energy Utilization, U.S. Dept. of Energy, April 18–21, 2005 [http://www.sc.doe.gov/bes/reports/files/SEU_rpt.pdf].
[2] M.A. Contreras, K. Ramanathan, J. AbuShama, F. Hasoon, D.L. Young, B. Egaas, R. Noufi, Prog. Photovolt: Res. Appl. 13 (2005) 209.
[3] A. Romeo, M. Terheggen, D. Abou-Ras, D.L. Bätzner, F.-J. Haug, M. Kälin, D. Rudmann, A.N. Tiwari, Prog. Photovolt: Res. Appl. 12 (2004) 93.
[4] M. Kemell, M. Ritala, M. Leskelä, Crit. Rev. Solid State Mater. Sci. 30 (2005) 1.
[5] M. Marudachalam, H. Hichri, R. Klenk, R.W. Birkmire, W.N. Shafarman, J.M. Schultz, Appl. Phys. Lett. 67 (1995) 3978.
[6] M. Kaelin, D. Rudmann, A.N. Tiwari, Solar Energy 77 (2004) 749.
[7] O. Ramdani, J.F. Guillemoles, D. Lincot, P.P. Grand, E. Chassaing, O. Kerrec, in: J. Portmans, H. Ossenbrink, E. Dunlop, P. Helm (Eds.), Proceedings of the 21st European Photovoltaic Solar Energy Conference, Dresden, Germany, September 4–8, 2006, p. 1866.
[8] M.E. Calixto, K.D. Dobson, B.E. McCandless, R.W. Birkmire, J. Electrochem. Soc. 153 (2006) G521.
[9] A. Kampmann, J. Rechid, A. Raitzig, S. Wulff, M. Mihhailova, R. Thyen, K. Kalberlah, Mater. Res. Soc. Symp. Proc. 763 (2003) B8.5.1.
[10] J.A. Hollingsworth, K.K. Banger, M.H.-C. Jin, J.D. Harris, J.E. Cowen, E.W. Bohannan, J.A. Switzer, W.E. Buhro, A.F. Hepp, Thin Solid Films 431–432 (2003) 63.
[11] S. Merdes, M. Sugiyama, M. Sano, Z. Hadjoub, H. Nakanishi, S. Ando, in: J. Portmans, H. Ossenbrink, E. Dunlop, P. Helm (Eds.), Proceedings of the 21st European Photovoltaic Solar Energy Conference, Dresden, Germany, September 4–8, 2006, p. 1870.
[12] M. Kaelin, H. Zogg, A.N. Tiwari, O. Wilhelm, S.E. Pratsinis, T. Meyer, A. Meyer, Thin Solid Films, 457 (2004) 391.
[13] A. Vervaet, M. Burgelman, I. Clemminck, M. Casteleyn, in: A. Luque, G. Sala, W. Palz, G. Dos Santos, P. Helm (Eds.), Proceedings of the 10th European Photovoltaic Solar Energy Conference, Lisbon, Portugal, April 8–12, 1991, p. 900.
[14] J.K.J. van Duren, C. Leidholm, A. Pudov, M.R. Robinson, Y. Roussillon, in: T. Gessert, K. Durose, C. Heske, S. Marsillac, T. Wada Thin-Film (Eds.), Compound Semiconductor Photovoltaics-2007, San Francisco, CA, April 9–13, 2007, Mater. Res. Soc. Sympos. Proc., 1012, 2007, Y05-03.
[15] V.K. Kapur, A. Bansal, P. Le, O.I. Asensio, Thin Solid Films 431–432 (2003) 53.
[16] D. B. Mitzi, M. Yuan, W. Liu, A. Kellock, S. Jay Chey, V. Deline, A. G. Schrott, Adv. Mater. 20 (2008) 3657.
[17] D.B. Mitzi, L.L. Kosbar, C.E. Murray, M. Copel, A. Afzali, Nature 428 (2004) 299.
[18] D.B. Mitzi, M. Copel, C.E. Murray, Adv. Mater. 18 (2006) 2448.
[19] D.J. Milliron, D.B. Mitzi, M. Copel, C.E. Murray, Chem. Mater. 18 (2006) 587.
[20] L. Weinhardt, O. Fuchs, D. Groß, E. Umbach, C. Heske, N.G. Dhere, A.A. Kadam, S.S. Kulkarni, J. Appl. Phys. 100 (2006) 024907.
[21] L.F. Audrieth, B. Ackerson Ogg, The Chemistry of Hydrazine, John Wiley & Sons, New York, 1951.
[22] R.N. Bhattacharya, J.F. Hiltner, W. Batchelor, M.A. Contreras, R.N. Noufi, J.R. Sites, Thin Solid Films 361–362 (2000) 396.
[23] T. Wada, N. Kohara, S. Nishiwaki, T. Negami, Thin Solid Films 387 (2001) 118.
[24] D. Abou-Ras, G. Kostorz, D. Bremaud, M. Kälin, F.V. Kurdesau, A.N. Tiwari, M. Döbeli, Thin Solid Films 480–481 (2005) 433.
[25] U. Rau, D. Braunger, R. Herberholz, H.W. Schock, J.-F. Guillemoles, L. Kronik, David Cahen, J. Appl. Phys. 86 (1999) 497.
[26] D. Cahen, R. Noufi, Appl. Phys. Lett. 54 (1989) 558.
[27] F.-J. Haug, D. Rudmann, H. Zogg, A.N. Tiwari, Thin Solid Films 431–432 (2003) 431.